



CHORUS

This is the accepted manuscript made available via CHORUS. The article has been published as:

# Grain Boundary Traction Signatures: Quantitative Predictors of Dislocation Emission

Ruizhi Li and Huck Beng Chew

Phys. Rev. Lett. **117**, 085502 — Published 15 August 2016

DOI: [10.1103/PhysRevLett.117.085502](https://doi.org/10.1103/PhysRevLett.117.085502)

## **Grain Boundary Traction Signatures: Quantitative Predictors of Dislocation Emission**

Ruizhi Li, Huck Beng Chew\*

Department of Aerospace Engineering, University of Illinois at Urbana-Champaign, Urbana, IL,  
USA

\*Author to whom all correspondence should be addressed. Email: [hbchew@illinois.edu](mailto:hbchew@illinois.edu)

First Author: Ruizhi Li,

Address: 104 S Wright Street, 324 Talbot Laboratory, Urbana IL 61801, USA

Second and Corresponding Author: Huck Beng Chew

Address: 104 S Wright Street, 306 H Talbot Laboratory, Urbana IL 61801, USA

Email: [hbchew@illinois.edu](mailto:hbchew@illinois.edu)

Tel: +1-217-333-9770

## **Abstract**

We introduce the notion of continuum-equivalent traction-fields as local quantitative descriptors of the grain boundary interface. These traction-based descriptors are capable of predicting the critical stresses to trigger dislocation emissions from ductile  $\langle 110 \rangle$  symmetrical-tilt nickel grain boundaries. We show that Shockley partials are emitted when the grain boundary tractions, in combination with external tensile loading, generate a resolved shear stress to cause dislocation slip. The relationship between the local grain boundary tractions and the grain boundary energy is established.

**Keywords:** mechanical strength; plasticity; dislocation emission; grain boundary structure; traction fields

Interfaces are ubiquitous in a wide range of natural and engineering materials, and affect many of the mechanical properties. It is well-accepted that the grain boundary interfaces control the strength and ductility of conventional polycrystalline metals by disrupting the motion of dislocations across grains [1]. In nanocrystalline metals, however, the grain boundaries also serve as sources for dislocation nucleation and emission [2-4]. For over 30 years, engineering the atomic structure of grain boundaries has been suggested as a viable means to improve the bulk mechanical properties of nanocrystalline metals. Much of our understanding of the relationship between the structure of a grain boundary and its propensity to emit dislocations has been provided by postdictive molecular dynamics (MD) simulations [5-8]. However, predicting the onset of plasticity directly from the equilibrium grain boundary atomic structure remains an unresolved challenge, due to the lack of a suitable quantitative descriptor of the grain boundary structure.

The grain boundary energy is a fundamental global quantity, but no correlation currently exists between the energy of the boundary and its ability to emit dislocations [9]. Studies have instead adopted structural unit (SU) models which divide the grain boundary region into distinct groups of atoms [10]. For  $\langle 110 \rangle$  symmetrical-tilt grain boundaries, for example, periodic arrays of four distinct SUs have been identified from four favored grain boundary orientations shown in Fig. 1A. Other grain boundaries can be represented by a combination of these four distinct SUs [11]. In metals with low stacking-fault energy, however, the extensive local atomic relaxations and delocalized grain boundary dislocations can produce grain boundary structures which are incompatible with the SU model description [8,11]. Even in cases when the delocalization is not too severe, the SUs within different grain boundary structures are not identical since they have varying degrees of distortion [12]. Nevertheless, grain boundaries containing E-SUs were found

to consistently emit dislocations at lower tensile stresses [7,13]. This peculiarity was attributed to the higher free volume of E-SU-containing grain boundaries, which allows atoms in the vicinity of the E-SUs to become more mobile due to lower electron density [14]. However, grain boundary porosity alone could not predict the critical stress required for the emission of dislocations.

To illustrate this issue, we create 16 bicrystal Ni <110> symmetrical-tilt grain boundary structures of varying tilt angles  $\theta$  in MD (see Supplement for modeling details). Each of these two-dimensional (2D) grain boundary structures is characterized by a repeating sequence of A, C, D, and/or E SUs along the  $x_1$  axis. We summarize the number and type of SUs as well as the number of pre-existing edge-type Shockley partials ( $b_1$ ) per grain boundary period  $d_p$  in Fig. 1B. We subject each bicrystal structure to uniaxial tensile deformation applied in the  $x_2$  direction perpendicular to the grain boundary until the first emission of dislocations. At this point, the stress-strain curves exhibit sudden loss of stress-carrying capacity (Supplement Fig. S1); the maximum tensile strength corresponds to the critical stress  $\sigma_{22}^c$  for dislocation nucleation and emission. Fig. 1C summarizes  $\sigma_{22}^c$  for the various grain boundary structures as a function of  $\theta$  (black symbols), as well as those for single crystal structures of the same orientation (blue symbols). Grain boundary structures of  $\theta < 115^\circ$  have high  $\sigma_{22}^c$  exceeding 12 GPa. In contrast, grain boundary structures of  $\theta > 115^\circ$  are inherently ductile, with  $\sigma_{22}^c$  falling to below 6 GPa. One explanation for this brittle-to-ductile transition is the presence of active dislocation sources in the form of E-SUs along the ductile grain boundaries (Fig. 1B) [7,14]. Aside from these E-SU-containing grain boundaries, certain grain boundary structures also contain pre-existing dislocations in the form of edge-type Shockley partials ( $b_1$ ). However, some of these structures are inherently brittle under tension (e.g.  $\Sigma 33(118)$ ,  $\Sigma 19(116)$ ), though one of them ( $\Sigma 33(554)$ )

has extremely low  $\sigma_{22}^c$  of  $\sim 2$  GPa. This indicates that the mere presence of dislocation sources along the grain boundary is not a sufficient gauge of its propensity to emit dislocations. In addition, the actual slip-system (magenta symbols in Fig. 1D) may not necessarily correspond to the one with the largest Schmid factor (black line) or the slip-system of pre-existing  $b_1$  partials along the grain boundaries (blue symbols). What makes certain grain boundaries more ductile than others? What governs the actual slip-system of these grain boundaries, and in turn  $\sigma_{22}^c$ ? Here, we show that the ductility of grain boundary structures can be accurately ascertained from continuum-equivalent traction-fields along the grain boundaries. Our traction-based predictions of  $\sigma_{22}^c$  (red symbols in Fig. 1C) compare very well with postdictive MD simulations (black symbols) for ductile grain boundaries of  $\theta > 115^\circ$ . The results are striking and exemplify the notion of continuum-equivalent traction fields as quantitative descriptors of the grain boundary atomic structures.

The local disruption of atoms from their bulk crystallographic arrangement near the grain boundary generates a stress-field which decays with distance from the boundary. We consider a plane-of-cut, with outer normal vector  $n_i$ , along the equilibrium grain boundary structure obtained from MD simulations. A distribution of tractions  $t_i$  has to be introduced along this plane-of-cut to maintain the same disruption of atoms caused by the presence of the grain boundary, and we take these tractions to represent the equilibrium grain boundary structure. Since these tractions are the equivalent forces per unit area acting across the grain boundary, they are related to the Cauchy stress tensor by  $t_i = \sigma_{ij}n_j$ . In MD, the virial definition of stress is often interpreted as the Cauchy equivalent stress. However, one cannot directly determine the grain boundary tractions from virial stress information along the grain boundary, since this information is only available at discrete atomic sites and provides an indication of stress only in

an averaged sense. Instead, we represent the continuous shear  $t_1$  and normal  $t_2$  traction distributions along the grain boundary with a Fourier series expansion, and extract the Fourier coefficients of these traction distributions inversely from local atomic stress information in the vicinity of the grain boundary using the virtual work principle (see Supplement and Fig. S2). The reconstructed grain boundary tractions are continuum-equivalent, since they satisfy both compatibility and equilibrium requirements.

We first examine the traction signatures along the ductile grain boundary structures with  $\theta > 115^\circ$ , where tensile deformation readily results in the emission of edge-type  $b_1$  Shockley partial dislocations from the boundaries. We focus only on the traction signatures associated with dislocation emissions into the upper grain. The plane-of-cut for these traction distributions are centered along the wall of the  $b_1$  partials in the case of  $\Sigma 33(554)$ , or near the relevant E-SUs along the grain boundary where slip first initiates, as denoted by yellow dashed lines in the equilibrium atomic configurations of three representative ductile grain boundaries in Fig. 2. Because of the translational symmetry of these grain boundary structures, similar traction signatures are observed along the green dashed lines in Fig. 2 for dislocation emissions into the lower grain.

The presence of pre-existing  $b_1$  partials is clearly evident for  $\Sigma 33(554)$  in Fig. 2A. In the vicinity of these  $b_1$  partials, both the continuum-equivalent normal and shear traction distributions fluctuate in sync, transitioning from negative to positive traction peaks of almost equal magnitude within a single atomic spacing. For clarity, we average these continuous traction distributions over the spacing of atoms along the boundary to obtain the atomic-scale average of the local normal and shear tractions, as denoted by the red open and blue cross symbols. The equal but opposite tractions generated on pairs of neighboring atoms centered at the dislocation

core of the  $b_1$  partial contributes to a shear-dominant loading along the close-packed  $\{111\}$  slip plane in the  $\langle 112 \rangle$  slip direction (inset in Fig. 2A). This non-trivial resolved shear stress arises solely from local tractions along an undeformed grain boundary structure, and allows one plane of atoms to slip more easily over its neighboring plane of atoms. This explains why  $\Sigma 33(554)$  grain boundaries are inherently ductile. Similar traction signatures are also observed along the  $\Sigma 11(332)$  grain boundary in Fig. 2B. The equal but opposite normal and shear tractions acting on neighboring pairs of atoms within the E-SUs create high resolved shear stress along the close-packed  $\{111\}\langle 112 \rangle$  slip system, while the initiation of slip is readily accommodated by the porous E-SUs; both these factors result in the high ductility of the  $\Sigma 11(332)$  grain boundary under tension. The  $\Sigma 33(441)$  grain boundary in Fig. 2C is notably wavy, and possesses high local shear stresses at the periodic wavy peaks and valleys due to local bending, as reflected in the  $t_1$  shear traction distribution. The emission of  $b_1$  partials is largely assisted by the resolved shear stress contribution from opposing  $t_2$  tractions on pairs of atoms along the boundary. The traction signatures of the ductile  $\Sigma 9(221)$ ,  $\Sigma 27(552)$  and  $\Sigma 19(331)$  grain boundaries represent intermediate cases that fall between the  $\Sigma 11(332)$  and  $\Sigma 33(441)$  grain boundaries, and are shown in Supplement Fig. S3.

The critical resolved shear stress  $\tau_c$  for emission of a  $b_1$  partial from the grain boundary has contributions from both the grain boundary normal and shear tractions, and external loading. To quantify the former, we perform a finite element analysis of an upper half space to represent the upper grain of the bicrystal structure, with imposed normal ( $t_2$ ) and shear tractions ( $t_1$ ) along the boundary from our continuum-equivalent traction distributions representing the grain boundary structure (see Supplement for modeling details). The upper half space is taken to be linear elastic with anisotropic properties of Ni corresponding to  $\theta$ , while the active  $\{111\}\langle 112 \rangle$  slip system

for pre-existing or nucleated  $b_1$  partials is modeled with a cohesive zone law (Fig. 3A). This cohesive zone law is fitted to the gradient of the generalized stacking fault energy (GSFE) of Ni along the  $\langle 112 \rangle$  partial dislocation slip direction computed from MD (Fig. 3B). From our finite element calculations (e.g.  $\Sigma 11(332)$  in Fig. 3C), we obtain the resolved shear stress contribution  $\tau_{GB}$  associated with the equivalent sliding-separation ( $\delta_{GB}$ ) along the slip plane (inset in Fig. 3C). For a partial dislocation to be emitted, the total resolved shear stress from contributions of both  $\tau_{GB}$  and external loading  $\tau_{ext} = m \sigma_{22}$  must exceed the critical barrier stress of  $\tau_0 \sim 5.1$  GPa for shear-slip (Fig. 3B), where  $\sigma_{22}$  is the applied tensile stress, and  $m$  is the Schmid factor of the slip-system associated with the  $b_1$  partial emission from the grain boundary. Hence, the predicted tensile strength of the grain boundary is  $\sigma_{22}^c = (\tau_0 - \tau_{GB})/m$ . We remark that the direction of  $b_1$  partial emission for the E-SU-containing grain boundaries can be ascertained from the lowest  $\sigma_{22}^c$  for the possible active slip-systems; this is in contrast to the operative slip-system for a bulk crystal lattice which corresponds to the one with the maximum Schmid factor.

We have calculated  $\tau_{GB}$ , and in turn the predicted  $\sigma_{22}^c$ , for the various grain boundary structures. For the ductile grain boundaries of  $\theta > 115^\circ$ , our traction-based predictions for  $\sigma_{22}^c$  (red symbols in Fig. 1C) are in perfect agreement with postdictive MD simulations (black symbols). These ductile grain boundary structures have either pre-existing Shockley partials, or have intact E-SUs where partial dislocations are readily emitted due to low nucleation stress. The brittle grain boundary structures of  $55^\circ < \theta < 100^\circ$  also contain pre-existing Shockley partials, and their traction signatures (Supplement Fig. S4) are very similar to the extremely ductile  $\Sigma 33(554)$  grain boundary in Fig. 2A. In the case of  $\Sigma 33(554)$ , the pre-existing Shockley partials are on slip-systems corresponding to the largest Schmid factor. In contrast, the pre-existing Shockley partials of all four grain boundary structures between  $55^\circ < \theta < 100^\circ$  are on slip-

systems with low Schmid factor of  $< 0.2$  (Fig. 1D). The deformation mechanisms of these grain boundary structures are not governed by dislocation processes due to the low Schmid factor, but instead involve phase boundary migration and grain rotation [8] which are outside the purview of the traction-based descriptor.

In the case of  $\Sigma 33(118)$  and  $\Sigma 19(116)$  grain boundaries, the pre-existing  $b_1$  partials are now on slip-systems with much higher Schmid factors. However, the traction signatures of these grain boundaries (Supplement Fig. S5) indicate a resolved shear stress contribution of  $\tau_{GB} < 0$  which opposes that generated by tensile loading; direct emission of the pre-existing  $b_1$  partials would require even higher tensile loads of  $(|\tau_{GB}| + \tau_0)/m$ . Hence, the local stress concentrators along the  $\Sigma 33(118)$  and  $\Sigma 19(116)$  grain boundaries actually prevent the emission of these grain boundary dislocations under tension. Such grain boundary structures are therefore inherently brittle under tension, but readily emit dislocations under compression. For these grain boundary structures, dislocation nucleates from within the bulk crystal lattice rather than from the grain boundaries under tension, and have different slip-systems from the pre-existing  $b_1$  partials along the grain boundaries (Fig. 1D).

The remaining grain boundary structures of  $\Sigma 11(113)$ ,  $\Sigma 9(114)$ ,  $\Sigma 27(115)$ , and the twin-boundary structure  $\Sigma 3(111)$  comprise of A, C, and/or D SUs, and do not have pre-existing  $b_1$  partials (Supplement Fig. S5). The A and D SUs are those of perfect face-centered-cubic (FCC) crystals and low-energy twin-boundaries, respectively, and are not sources for dislocation nucleation under tension. The C SUs are lattice dislocations with  $\frac{1}{2}[110]$  cores in the out-of-plane direction [15]. Hence, there are no active dislocation sources along these grain boundary

structures to allow emission in the in-plane directions under tension, which explains why these structures have comparable tensile strength to their single crystal counterparts (Fig. 1C).

Our above results demonstrate that the continuum-equivalent traction-fields are local grain boundary descriptors. These grain boundary  $t_1, t_2$  tractions will have associated  $u_1, u_2$  separations along the grain boundary as a work-conjugate. For grain boundaries with active dislocation sources, i.e. pre-existing Shockley partials or E-SUs, we compute the  $u_1, u_2$  local separation distributions via the displacements of the deformed half-space in our finite element model with cohesive zones representing the active slip-systems (Fig. 3C). In the absence of active dislocation sources, i.e.  $\Sigma 11(113), \Sigma 9(114), \Sigma 27(115)$  and  $\Sigma 3(111)$ , these separation distributions are computed from a finite element half-space without cohesive zones. Then, the traction energy defined by  $\int \mathbf{u} \cdot \mathbf{t} dx_1$ , accounting for contributions from both the upper and lower half-spaces (grains), represents the energy contribution from the local disruption in the bulk crystallographic arrangement of atoms outside the core structure of the grain boundary (e.g. outside of the dashed yellow and green lines in Fig. 2). This traction energy is primarily responsible for the generation of (a) an elastic stress-field which decays with distance from the boundary, as well as (b) a resolved shear stress along the  $\langle 112 \rangle$  crystal orientations for grain boundaries with active dislocation sources. In addition to the traction energy, there is also a structural energy component which can be delineated into the structural energies of the A, C, D and E SUs, as well as the stacking fault energy and dislocation core energy of any pre-existing  $b_1$  partial. See Supplement for calculation details. The combined contribution of the structural and traction energies then constitutes the global descriptor – the grain boundary energy, as shown in Fig. 4. Observe that the structural energy is a major component of the grain boundary energy, but this component is not directly responsible for emission of dislocations from the grain boundary

structure. Even from the traction energies, one cannot discern if the grain boundary structures are ductile or brittle, thus local grain boundary descriptors are required. This explains the poor correlation between grain boundary energy and the mechanical properties [7,9].

In summary, we have shown that grain boundary traction-fields are capable of quantitatively predicting the critical stresses to trigger dislocation emissions across all ductile symmetrical-tilt  $\langle 110 \rangle$  Ni grain boundary structures. Such descriptors allow us to accurately ascertain the strength and ductility of a grain boundary directly from its atomic structure. The establishment of traction-based grain boundary descriptors is broadly applicable to predicting the deformation mechanics in complex interface structures subjected to a variety of loading conditions. This has important implications in the predictive rather than postdictive design and engineering of grain boundaries.

### **Acknowledgements**

The authors acknowledge the support provided by Dr. Ali Sayir under the AFOSR Aerospace Materials for Extreme Environment Program (award no. FA9550-15-1-0117), as well as computational time provided by TACC (award no. TG-MSS130007) and the Blue Waters sustained-petascale computing project which is supported by the National Science Foundation (awards OCI-0725070 and ACI-1238993) and the state of Illinois. Blue Waters is a joint effort of the University of Illinois at Urbana-Champaign and its National Center for Supercomputing Applications.

### **References**

1. J. Kacher, B. P. Eftink, B. Cui, and I. M. Robertson, *Curr. Opin. Solid State Mater. Sci.* **18**, 227 (2014).
2. V. Yamakov, D. Wolf, S. R. Phillpot, A. K. Mukherjee, and H. Gleiter, *Nat. Mater.* **1**, 45 (2002).
3. Z. Shan, E. A. Stach, J. M. Wiezorek, J. A. Knapp, D. M. Follstaedt, and S. X. Mao, *Science* **305**, 654 (2004).

4. X. Y. Li, Y. J. Wei, L. Lu, K. Lu, and H. J. Gao, *Nature* **464**, 877 (2010).
5. M. D. Sangid, T. Ezaz, H. Sehitoglu, and I.M. Robertson, *Acta Mater.* **59**, 283 (2011).
6. M. A. Tschopp, and D. L. McDowell, *Scrip. Mater.* **58**, 299 (2008).
7. M. A. Tschopp, G. J. Tucker, and D. L. McDowell, *Acta Mater.* **55**, 3959 (2007).
8. J. Wang, A. Misra, and J. P. Hirth, *Phys. Rev. B* **83**, 064106(2011).
9. D. L. Olmsted, S. M. Foiles, and E. A. Holm, *Acta Mater.* **57**, 3694 (2009).
10. A. P. Sutton, and V. Vitek, *Phil. Trans. R. Soc. A* **309**, 1 (1983).
11. J. D. Rittner, and D. N. Seidman, *Phys. Rev. B* **54**, 6999 (1996).
12. R. W. Balluffi, and P. D. Bristowe, *Surf. Sci.* **144**, 28 (1984).
13. D. E. Spearot, M. A. Tschopp, K. I. Jacob, and D. L. McDowell, *Acta Mater.* **55**, 705 (2007).
14. G. J. Tucker, M. A. Tschopp, and D. L. McDowell, *Acta Mater.* **58**, 6464 (2010).
15. T. Shimokawa, *Phys. Rev. B* **82**, 174122 (2010).

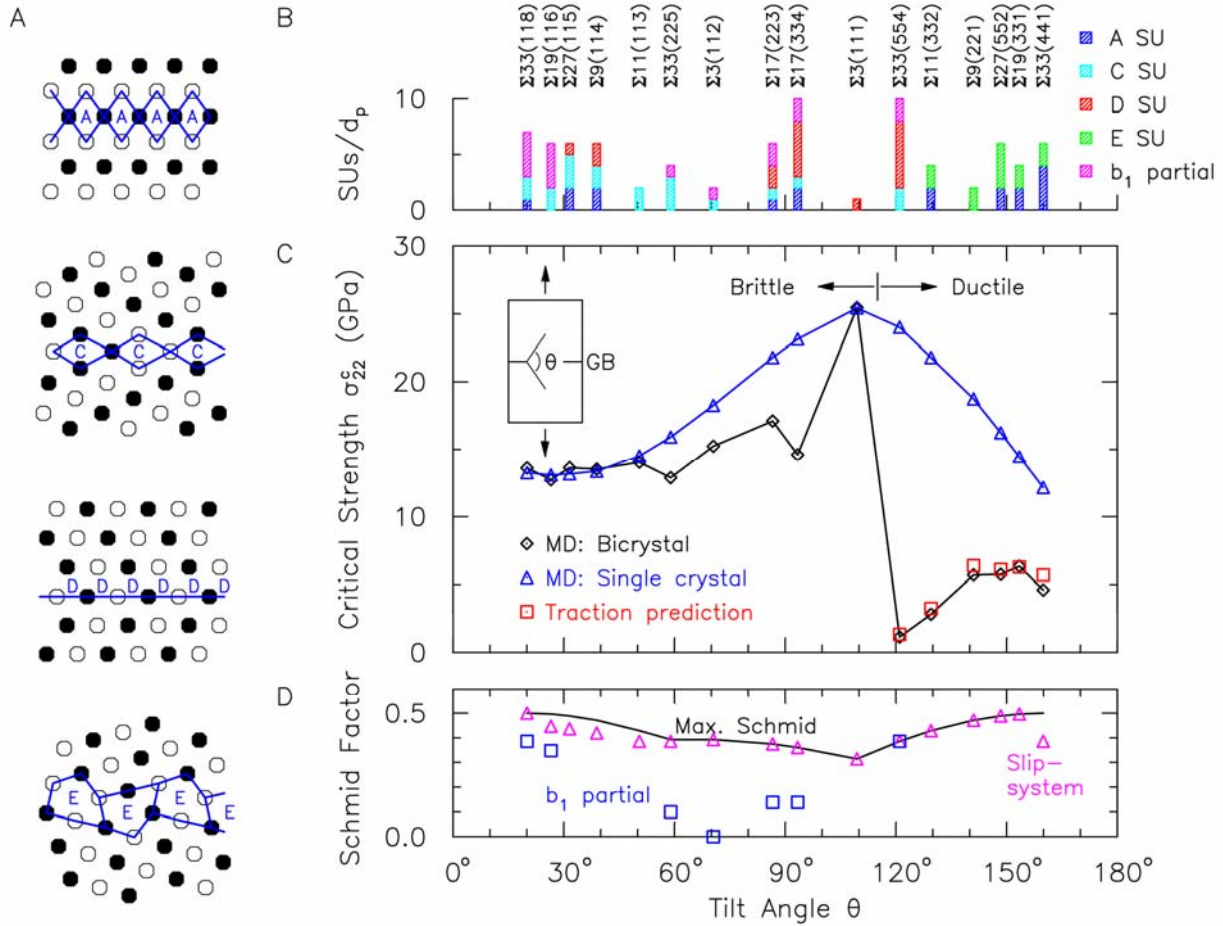


**Fig. 1.** (A) Periodic arrays of the A, C, D, and E structural units (SUs) along four favored  $\langle 110 \rangle$  symmetrical-tilt grain boundaries:  $\Sigma 1(110)$ ,  $\Sigma 11(113)$ ,  $\Sigma 3(111)$ , and  $\Sigma 9(221)$ . (B) Count of SUs and edge-type Shockley partials ( $b_1$ ) within a single grain boundary period ( $d_p$ ) of the Ni  $\langle 110 \rangle$  symmetrical-tilt grain boundary structures. (C) Critical tensile strength for emission of Shockley partials ( $\sigma_{22}^c$ ) versus grain boundary tilt angle ( $\theta$ ) from MD simulations and traction-based predictors. (D) Maximum Schmid factor, and the Schmid factors of actual slip-systems and slip-systems of pre-existing  $b_1$  partials, versus  $\theta$ .

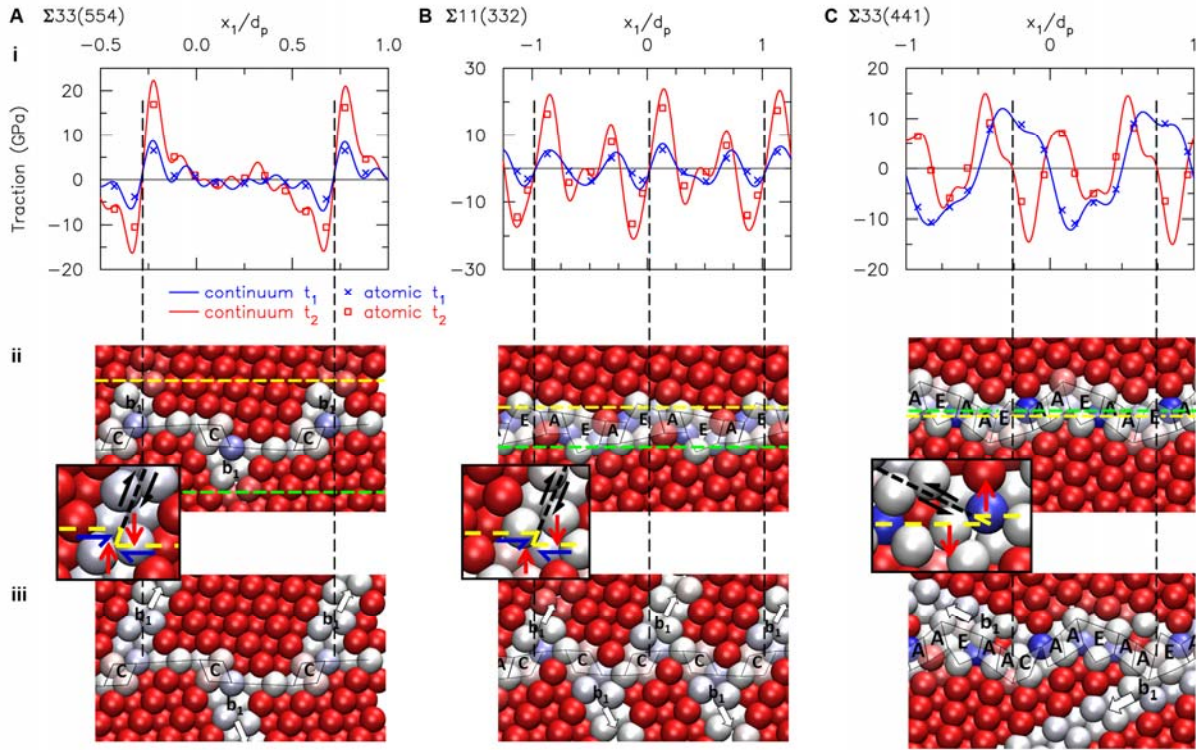


**Fig. 2.** Traction-signatures along (A)  $\Sigma 33(554)$ , (B)  $\Sigma 11(332)$ , and (C)  $\Sigma 33(441)$  ductile grain boundaries. (i) Continuum-equivalent normal and shear traction distributions (lines), which are averaged over the atomic spacing along the boundary to obtain the atomic-scale tractions (symbols). (ii) Atomic configurations of the equilibrium grain boundary structure. (iii) Atomic configurations of the deformed grain boundary structure at the first instant of  $b_1$  partial emission. Atoms in (ii) and (iii) are colored by their centro-symmetry parameter. Intersections between the yellow and black dashed lines in (ii) denote the sites for  $b_1$  partial emission into the upper grain. Close-up views of the deformed configurations in the insets in (ii): red and blue arrows denote the normal and shear tractions on atom pairs at the origin of dislocation slip; black arrows denote the resolved shear stress contribution from the grain boundary tractions.

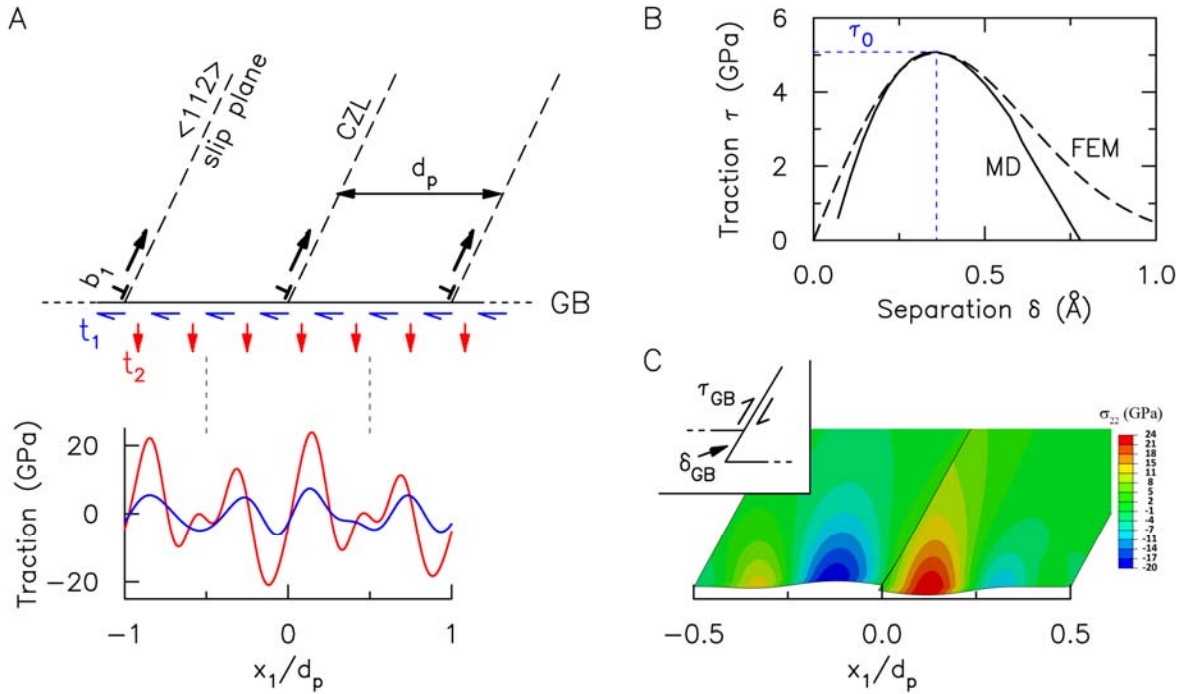


**Fig. 3.** Resolved shear stress contributions from grain boundary tractions. **(A)** Schematic of the finite element model of an upper half-space with imposed grain boundary tractions to represent the upper grain; cohesive zone laws (CZL) along the emission path account for slip of the  $b_1$  partials. **(B)** Cohesive zone law calibrated from MD for slip of a  $b_1$  partial in the  $\langle 112 \rangle$  direction. **(C)** Finite element calculations of the deformed geometry of the equilibrium  $\Sigma 11(332)$  grain boundary structure with displayed contours of the  $\sigma_{22}$  stress; schematic of the resolved shear stress  $\tau_{GB}$  and associated sliding-separation  $\delta_{GB}$  along the slip-plane in the inset.

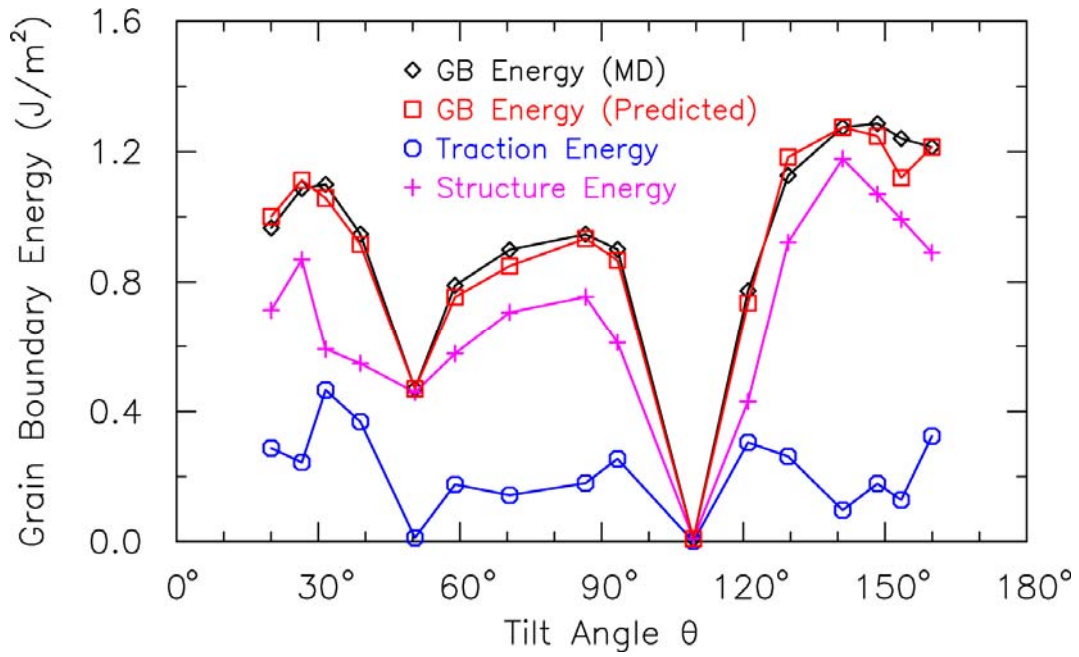


**Fig. 4.** Grain boundary energy of the Ni <110> symmetrical-tilt grain boundary structures, delineated into traction and structural energy contributions.